OPEN ACCESS

University of BRISTOL

Karuppiah, V., Ranaghan, K., Leferink, N. G. H., Johannissen, LO., Shanmugam, M., Cheallaigh, A. N., ... Scrutton, NS. (2017). Structural basis of catalysis in the bacterial monoterpene synthases linalool synthase and 1,8-cineole synthase. *ACS Catalysis*, *7*(9), 6268-6282. https://doi.org/10.1021/acscatal.7b01924

Peer reviewed version

Link to published version (if available):
10.1021/acscatal.7b01924

Link to publication record in Explore Bristol Research
PDF-document

This is the author accepted manuscript (AAM). The final published version (version of record) is available online via ACS at http://pubs.acs.org/doi/10.1021/acscatal.7b01924. Please refer to any applicable terms of use of the publisher.

University of Bristol - Explore Bristol Research

General rights

This document is made available in accordance with publisher policies. Please cite only the published version using the reference above. Full terms of use are available:
http://www.bristol.ac.uk/pure/about/ebr-terms

Supporting information

Structural basis of catalysis in the bacterial monoterpene synthases linalool synthase and 1,8-cineole synthase

Vijaykumar Karuppiah,[†] Kara E. Ranaghan,[‡] Nicole G. H. Leferink,[†] Linus O. Johannissen,[†] Muralidharan Shanmugam,[†] Aisling Ní Cheallaigh,[†] Nathan J. Bennett,[†] Lewis J. Kearsey,[†] Eriko Takano,[†] John M. Gardiner,[†] Marc W. van der Kamp,[‡] Sam Hay,[†] Adrian J. Mulholland,[‡] David Leys[†] and Nigel S. Scrutton[,†]*

† BBSRC/EPSRC Manchester Synthetic Biology Research Centre for Fine and Specialty Chemicals (SYNBIOCHEM), Manchester Institute of Biotechnology, School of Chemistry, Faculty of Science and Engineering, University of Manchester, 131 Princess Street, Manchester M1 7DN, U.K.

‡ Centre for Computational Chemistry, School of Chemistry, University of Bristol, Cantock's Close, Bristol BS8 1TS, U.K.

*Corresponding author. Email: Nigel.Scrutton@manchester.ac.uk

Table of contents

Extended EPR results and discussion

Extended EPR results and discussion

Comparisons of EPR spectra of Mn^{2+} ion substituted bCinS/bLinS with and without FGPP along with standard $MnCl_2$ samples show a clearly resolved multiplet structure for 1:1 bCinS/bLinS: $MnCl_2$ in the presence of FGPP. The observation of a multiplet structure indicates that degeneracy of the six-line EPR spectrum, often associated with free/unbound Mn^{2+} ion, was either lifted by the strong zero-field splitting of the Mn^{2+} ion or the '*g*-anisotropy' or combination of both (**Figure 3**; black asterisks). The intense EPR transitions centered around g ~ 2.0 (**Figure 3**; black/blue asterisks) were mainly due to the transitions from $|m_s, -½\rangle \rightarrow |m_s, +½\rangle$ manifold. The weak hyperfine structures that appear above and below the $g \sim 2.0$ region (**Figure 3**; blue arrows) are due to the transitions between the higher spin manifolds, $|m_s, -5/2\rangle \rightarrow |m_s, -3/2\rangle$ and $|m_s, -3/2\rangle \rightarrow |m_s, -½\rangle$ respectively. The multiplet structure observed for bCinS and bLinS directly probes the local/first coordination sphere of the Mn^{2+} ion, which was clearly different from the reference samples $[Mn(H_2O)_6]^{2+}$ (black dotted spectrum) and bCinS/bLinS without FGPP (black dashed spectrum). The aforementioned two samples predominantly showed a six-line EPR pattern with half-field transitions in the range of 80-150 mT, whereas for 1:1 bCinS/bLinS-FGPP: $MnCl_2$, it occurred between 120-180 mT and trailed towards high magnetic field (**Figures S6 and S7**). The intensity of the multiplet structure and the half-field transitions between 120-180 mT (**Figures S6 and S7**; red downward arrows) remained as a plateau for the samples when the concentration of the Mn^{2+} ion relative to bCinS-FGPP/bLinS-FGPP was more than 3. The presence of additional equivalents of Mn^{2+} ion was observed as free/unbound Mn^{2+} ion, which predominantly contributes to the six-line EPR pattern around the $g = 2$ region (**Figure 3**; black asterisks). In addition, new half-field transitions were observed at low magnetic fields between 80-150 mT (**Figures S6 and S7**; blue arrows) and the intensity increased linearly. The observed half-field transitions were consistent with the free/unbound Mn^{2+} ion EPR signal. All these observations are consistent with bCinS and bLinS having 3 metal binding sites.

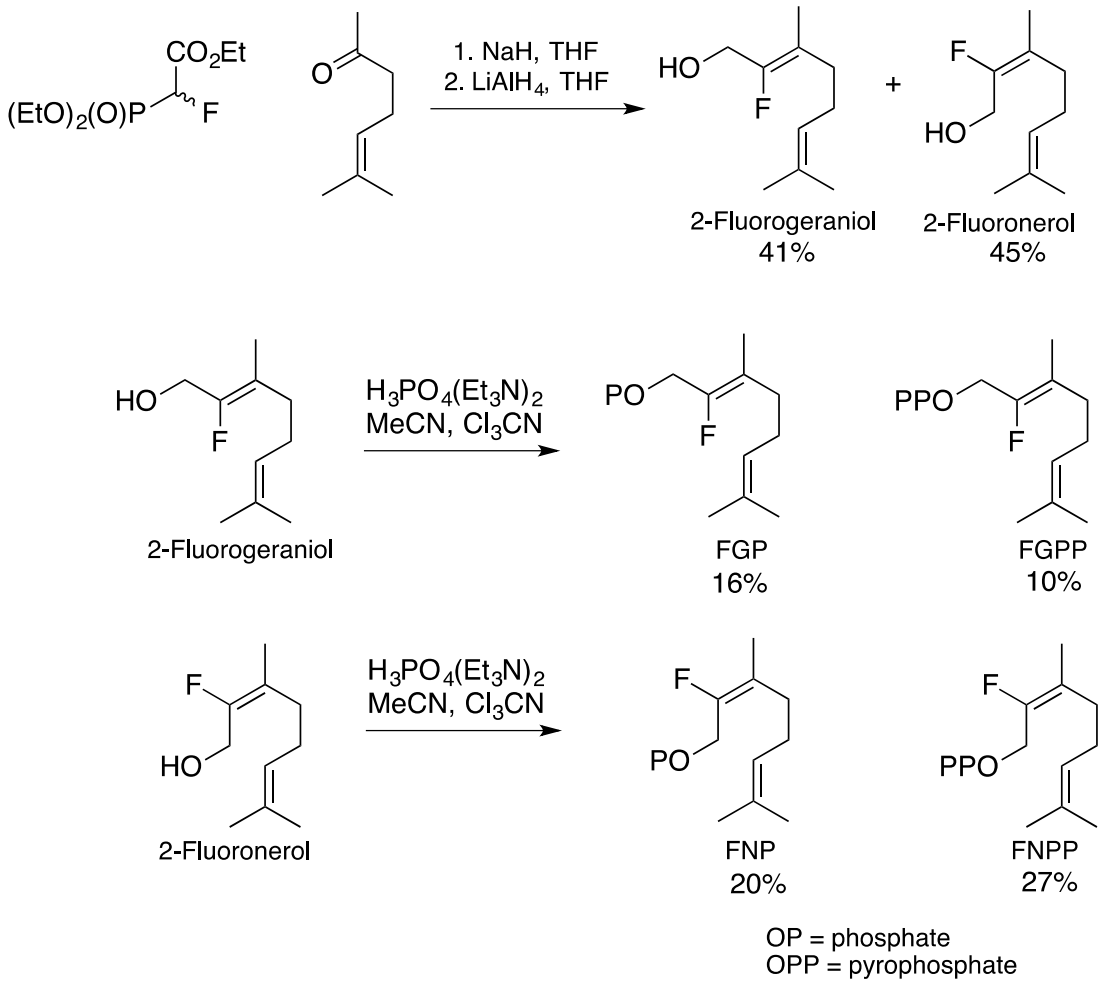

Scheme S1: Synthesis of FGP, FGPP, FNP and FNPP.

A

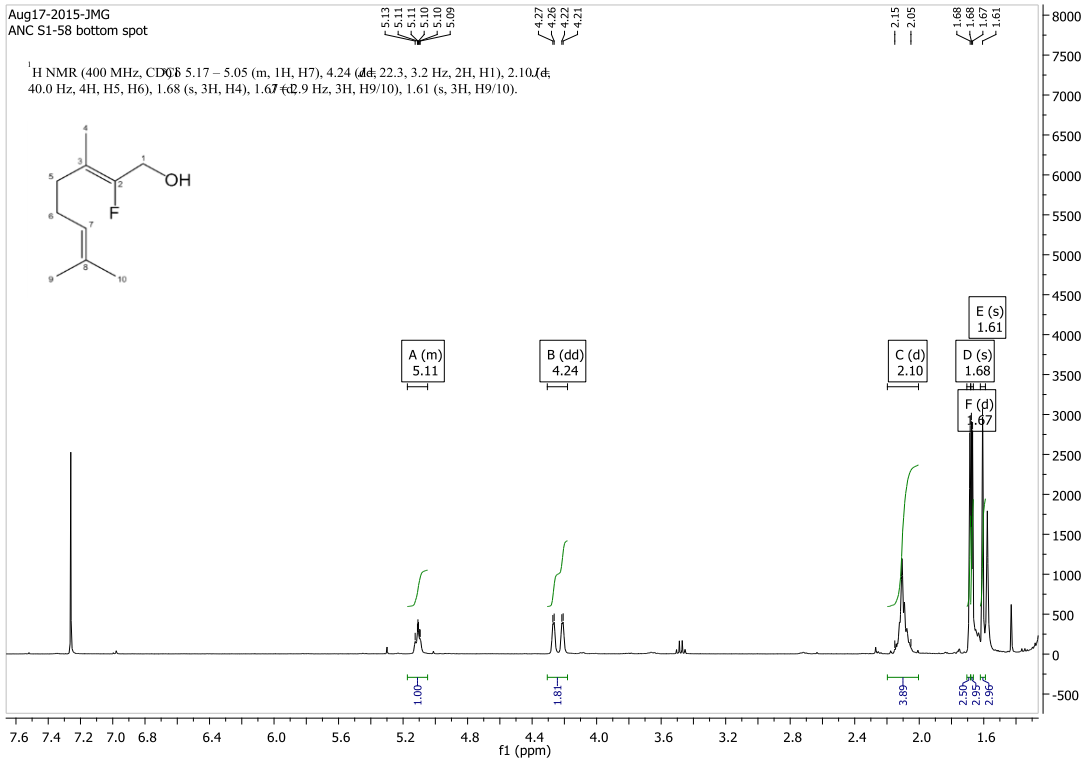

^{1}H NMR (400 MHz, CDCl$_3$) δ 5.17 – 5.05 (m, 1H, H7), 4.24 (dd, J = 22.3, 3.2 Hz, 2H, H1), 2.10 (d, J = 40.0 Hz, 4H, H5, H6), 1.68 (s, 3H, H4), 1.67 (d, J = 2.9 Hz, 3H, H9/10), 1.61 (s, 3H, H9/10).

B

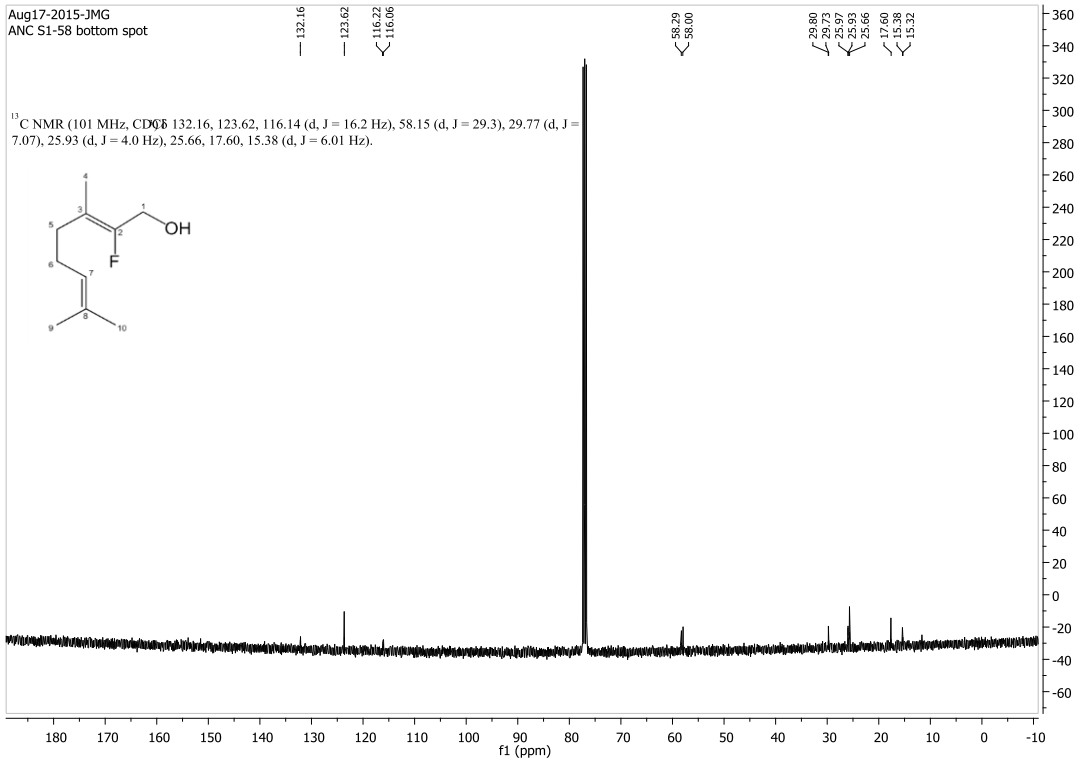

^{13}C NMR (101 MHz, CDCl$_3$) δ 132.16, 123.62, 116.14 (d, J = 16.2 Hz), 58.15 (d, J = 29.3), 29.77 (d, J = 7.07), 25.93 (d, J = 4.0 Hz), 25.66, 17.60, 15.38 (d, J = 6.01 Hz).

C

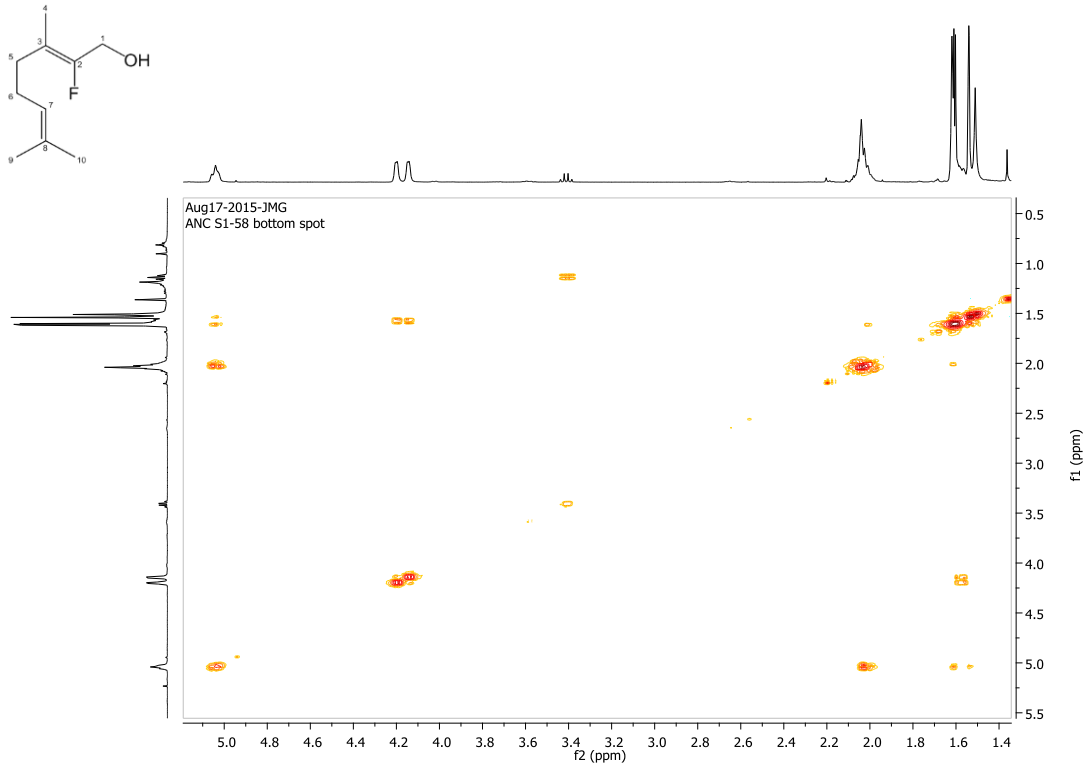
OH
F
Aug17-2015-JMG
ANC S1-58 bottom spot
f2 (ppm)
f1 (ppm)

D

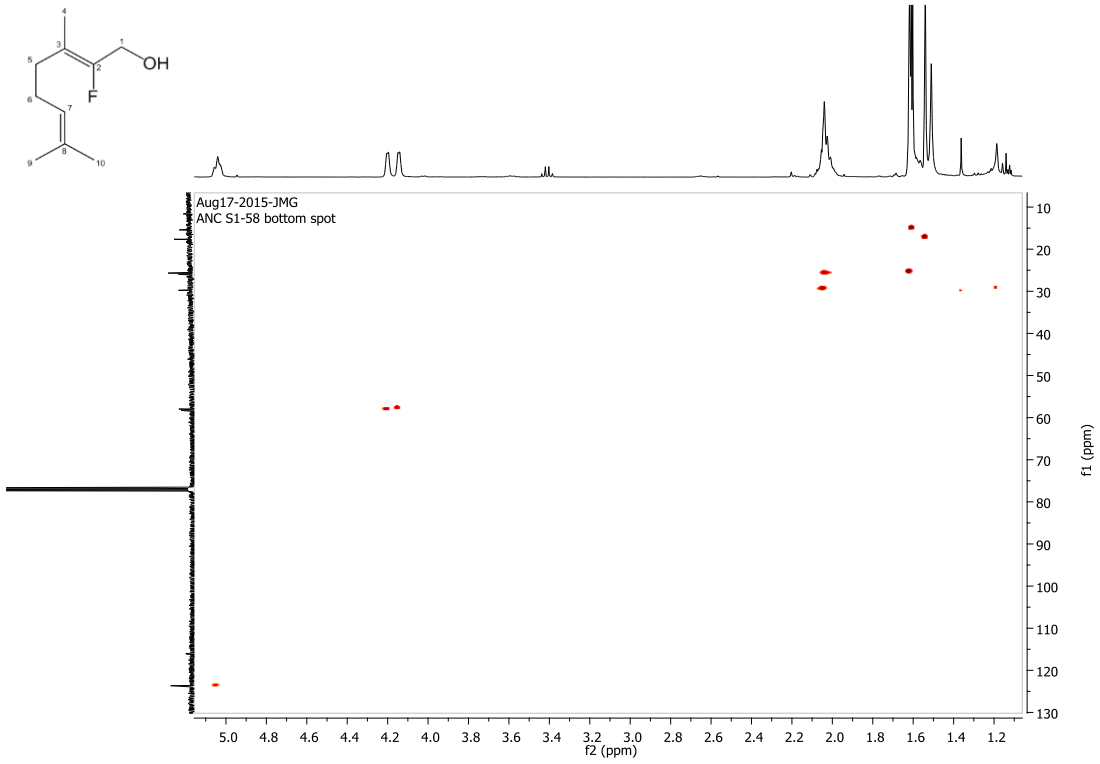
OH
F
Aug17-2015-JMG
ANC S1-58 bottom spot
f2 (ppm)
f1 (ppm)

E

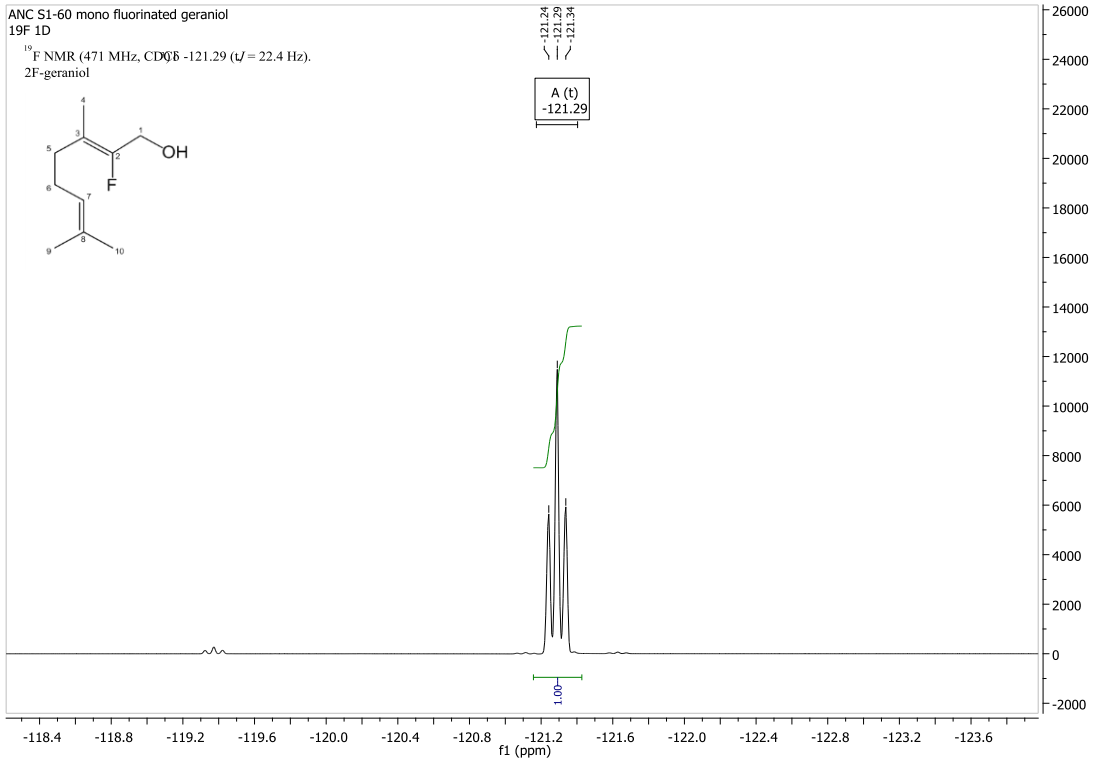

Figure S1. NMR spectra of 2-fluorogeraniol. A) ^{1}H NMR. B) ^{13}C NMR. C) ^{1}H - ^{1}H COSY. D) ^{1}H -^{13}C HSQC. E) ^{19}F NMR.

A

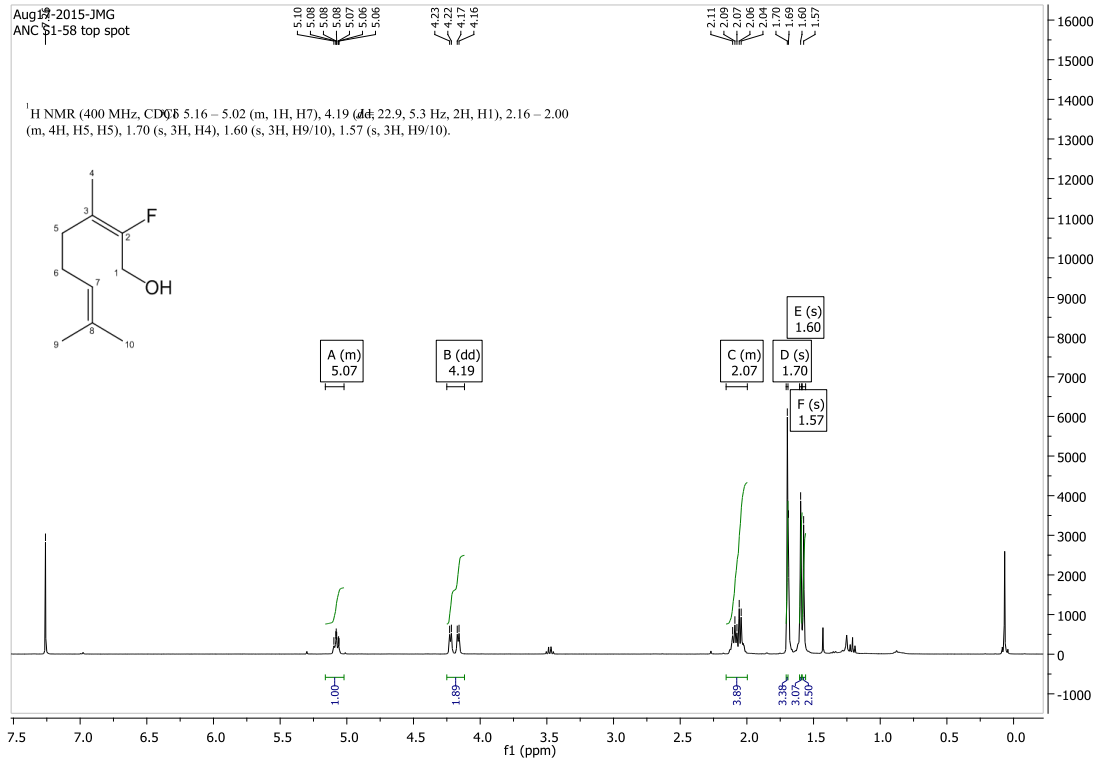
Aug17-2015-JMG
ANC S1-58 top spot
5.10 5.08 5.08 5.08 5.07 5.06 5.06 5.06
4.23 4.22 4.17 4.16
2.11 2.09 2.07 2.06 2.04 1.70 1.69 1.60 1.57
1H NMR (400 MHz, CDCl3) δ 5.16 – 5.02 (m, 1H, H7), 4.19 (dd, J = 22.9, 5.3 Hz, 2H, H1), 2.16 – 2.00 (m, 4H, H5, H5), 1.70 (s, 3H, H4), 1.60 (s, 3H, H9/10), 1.57 (s, 3H, H9/10).
F
OH
A (m) 5.07
B (dd) 4.19
C (m) 2.07
D (s) 1.70
E (s) 1.60
F (s) 1.57
1.00 1.89 3.89 3.38 3.07 2.50
f1 (ppm)

B

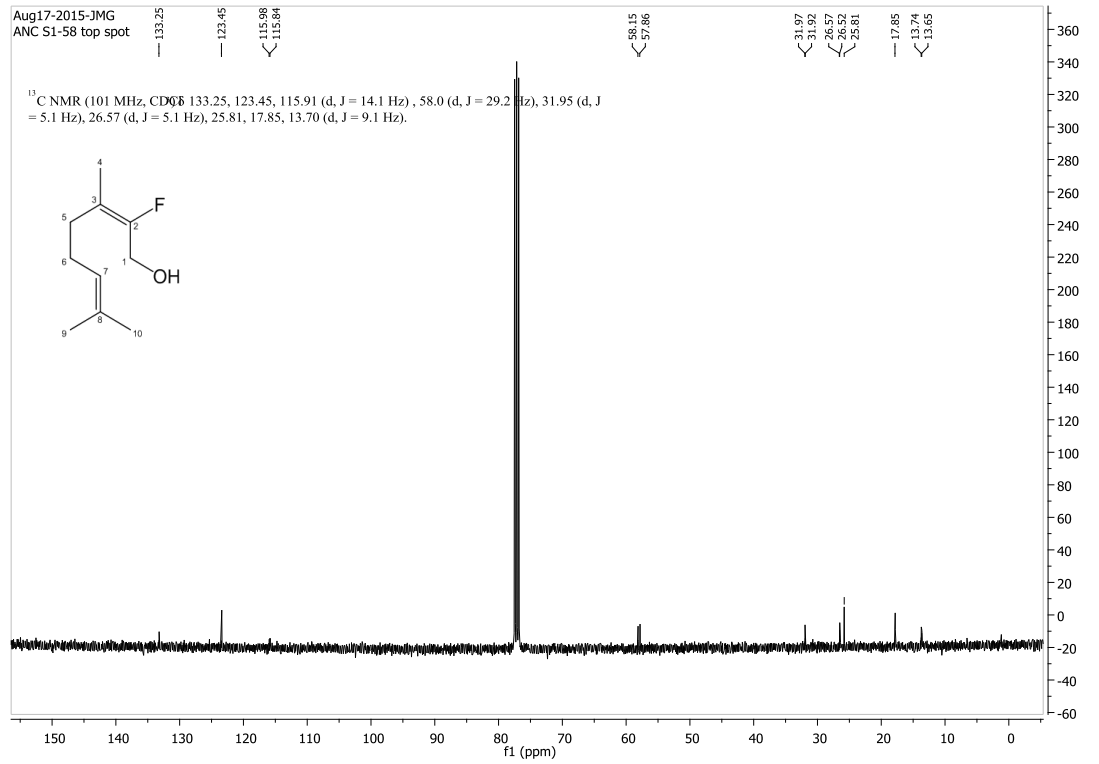
Aug17-2015-JMG
ANC S1-58 top spot
133.25 123.45 115.98 115.84 58.15 57.86 31.97 31.92 26.57 26.52 25.81 17.85 13.74 13.65
13C NMR (101 MHz, CDCl3) δ 133.25, 123.45, 115.91 (d, J = 14.1 Hz) , 58.0 (d, J = 29.2 Hz), 31.95 (d, J = 5.1 Hz), 26.57 (d, J = 5.1 Hz), 25.81, 17.85, 13.70 (d, J = 9.1 Hz).
F
OH
f1 (ppm)

C

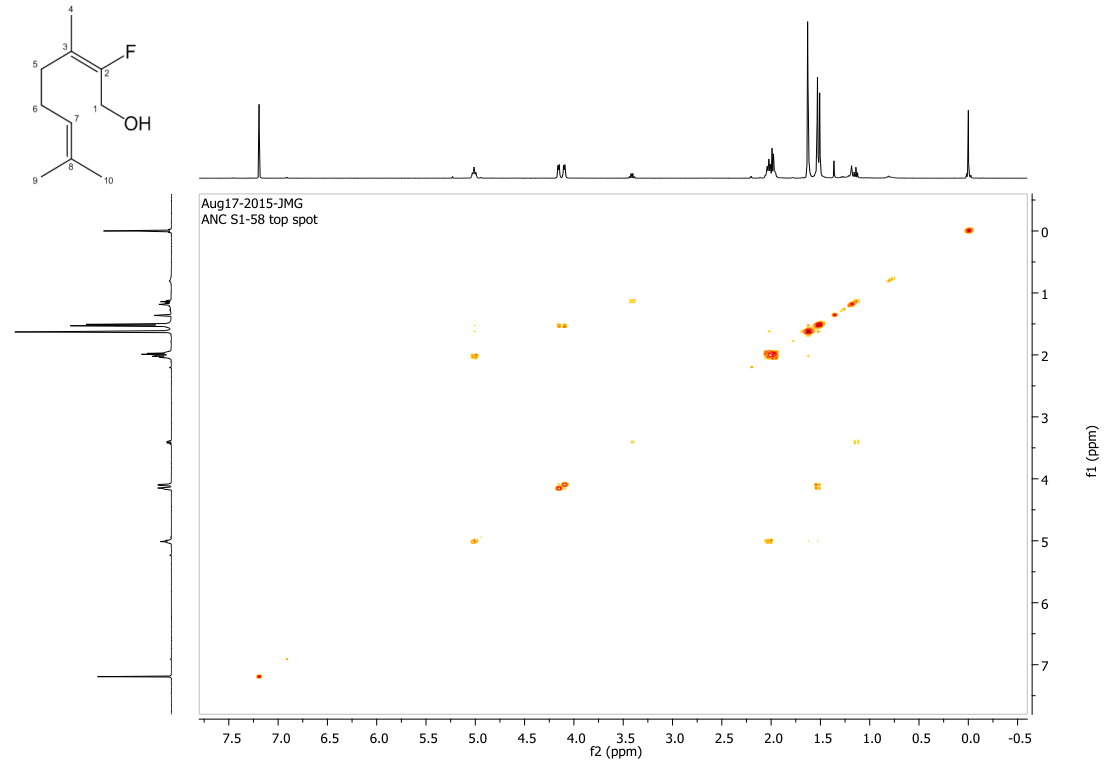
F
OH
Aug17-2015-JMG
ANC S1-58 top spot
f2 (ppm)
f1 (ppm)

D

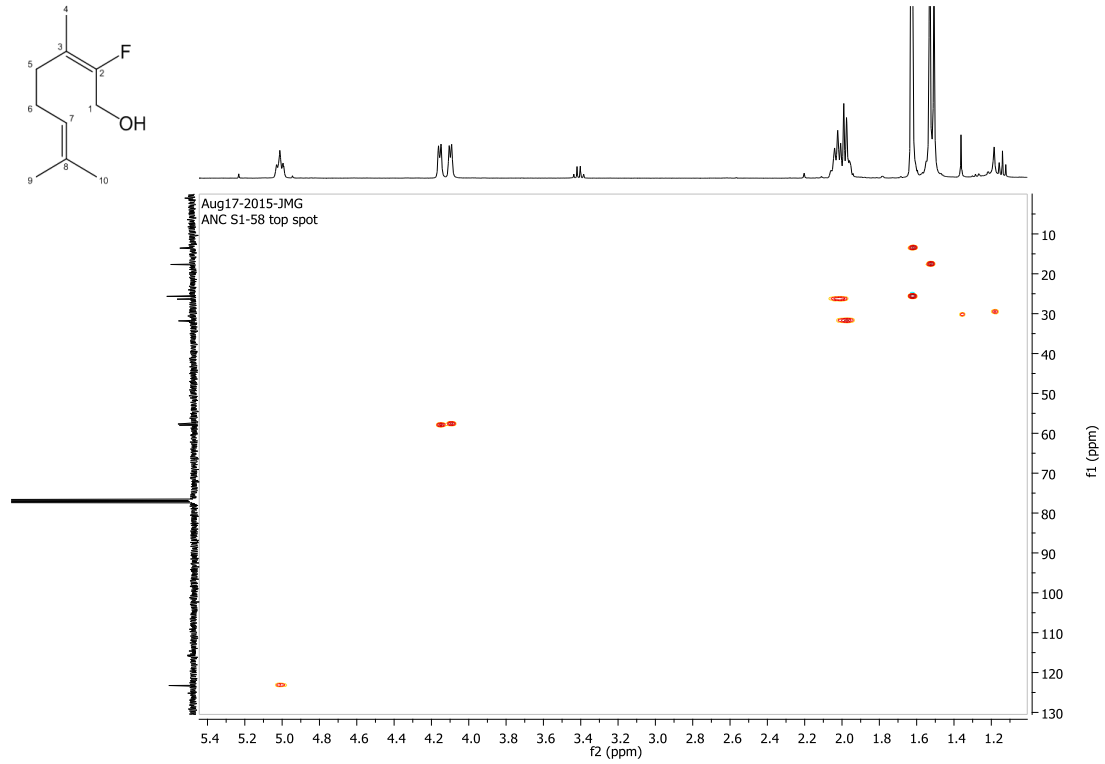
F
OH
Aug17-2015-JMG
ANC S1-58 top spot
f2 (ppm)
f1 (ppm)

E

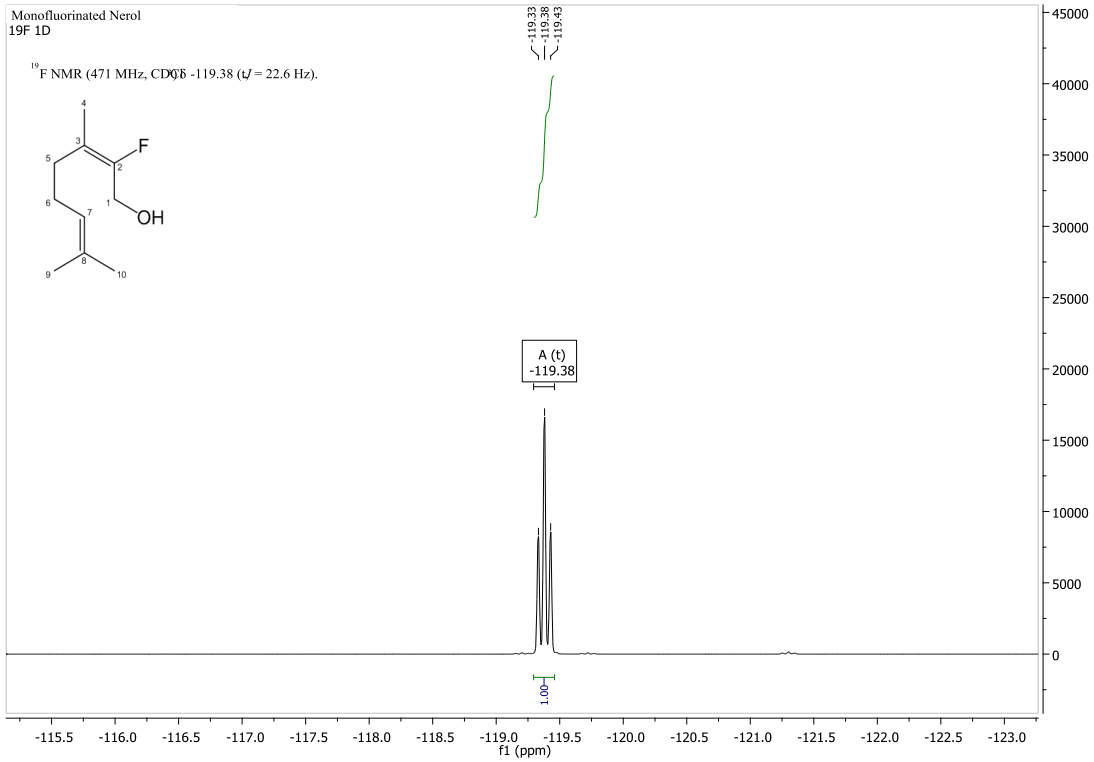

Figure S2. NMR spectra of 2-fluoronerol. A) ^{1}H NMR. B) ^{13}C NMR. C) ^{1}H -^{1}H COSY. D) ^{1}H -^{13}C HSQC. E) ^{19}F NMR.

A

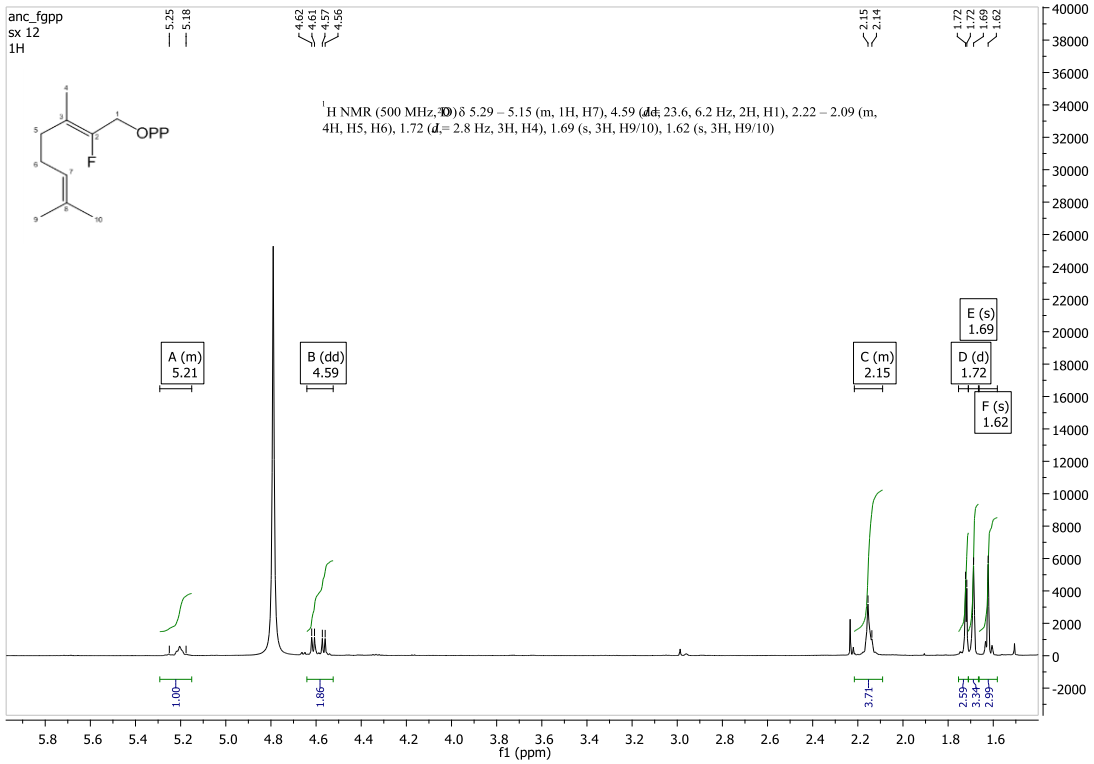
anc_fgpp
sx 12
1H
5.25
5.18
4.62
4.61
4.57
4.56
2.15
2.14
1.72
1.72
1.69
1.62
OPP
F
^{1}H NMR (500 MHz, 2O) δ 5.29 – 5.15 (m, 1H, H7), 4.59 (dd, J = 23.6, 6.2 Hz, 2H, H1), 2.22 – 2.09 (m, 4H, H5, H6), 1.72 (d, J = 2.8 Hz, 3H, H4), 1.69 (s, 3H, H9/10), 1.62 (s, 3H, H9/10)
A (m) 5.21
B (dd) 4.59
C (m) 2.15
D (d) 1.72
E (s) 1.69
F (s) 1.62
1.00
1.86
3.71
2.59
3.34
2.99
f1 (ppm)

B

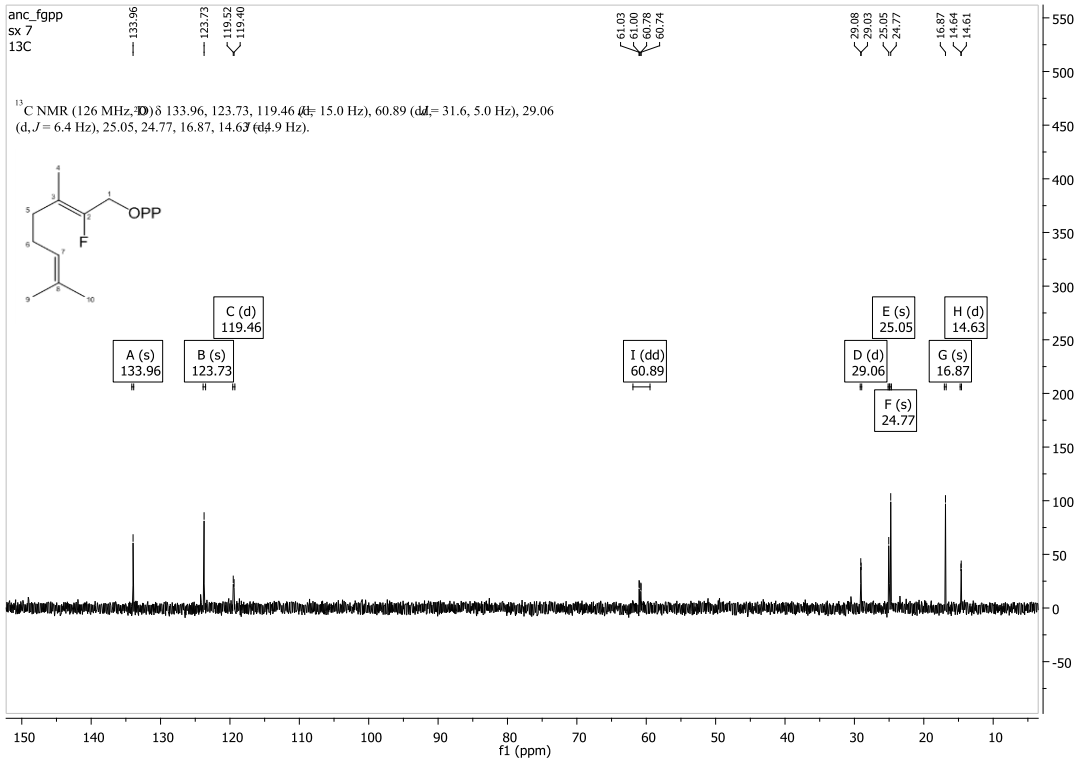
anc_fgpp
sx 7
13C
133.96
123.73
119.52
119.40
61.03
61.00
60.78
60.74
29.08
29.03
25.05
24.77
16.87
14.64
14.61
OPP
F
^{13}C NMR (126 MHz, 2O) δ 133.96, 123.73, 119.46 (d, J = 15.0 Hz), 60.89 (dd, J = 31.6, 5.0 Hz), 29.06 (d, J = 6.4 Hz), 25.05, 24.77, 16.87, 14.63 (d, J = 4.9 Hz).
A (s) 133.96
B (s) 123.73
C (d) 119.46
I (dd) 60.89
D (d) 29.06
E (s) 25.05
F (s) 24.77
G (s) 16.87
H (d) 14.63
f1 (ppm)

C

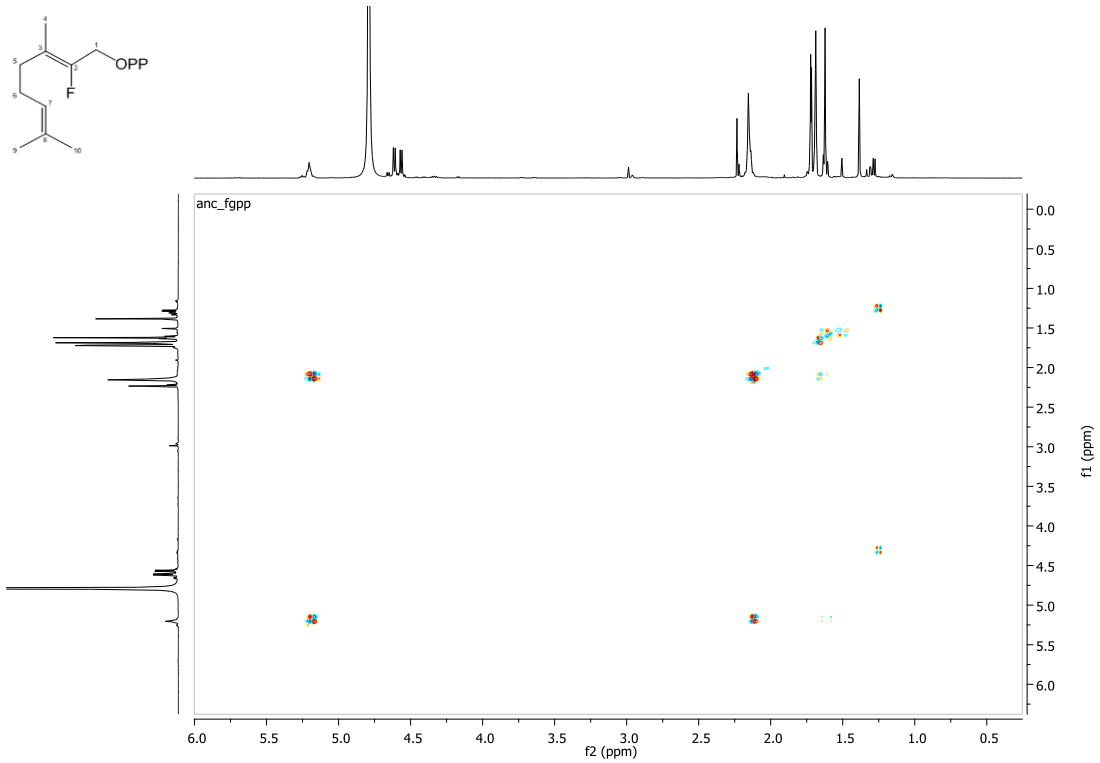

D

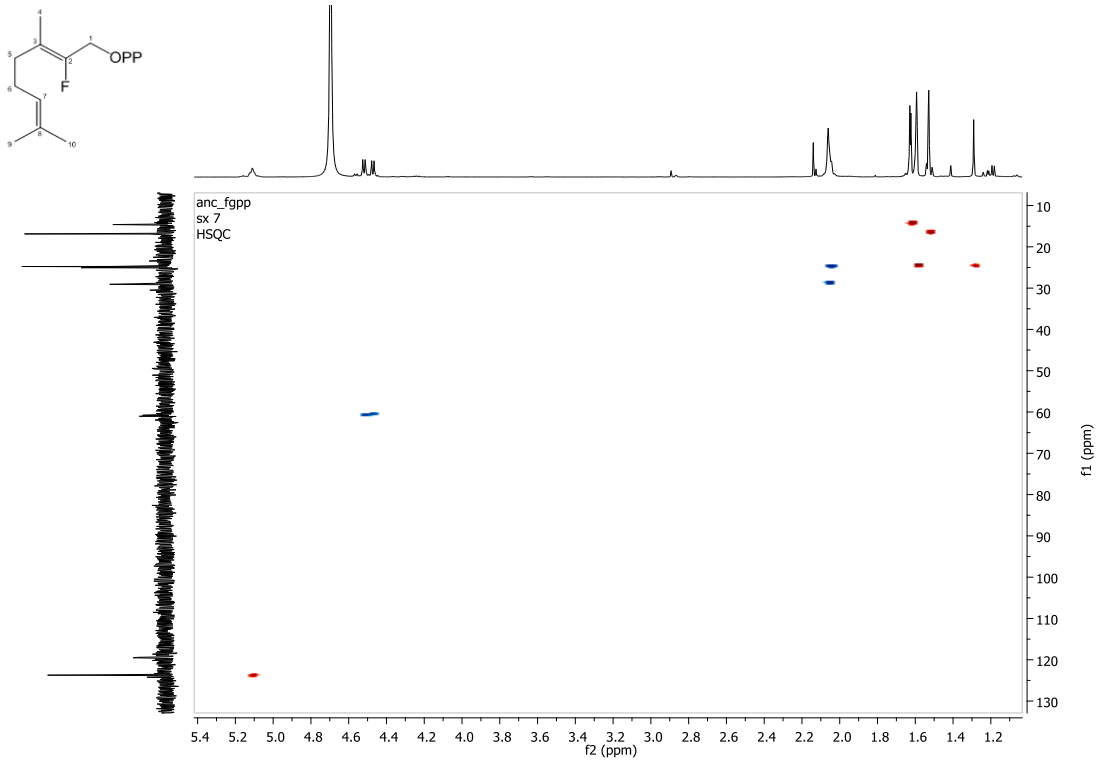

E

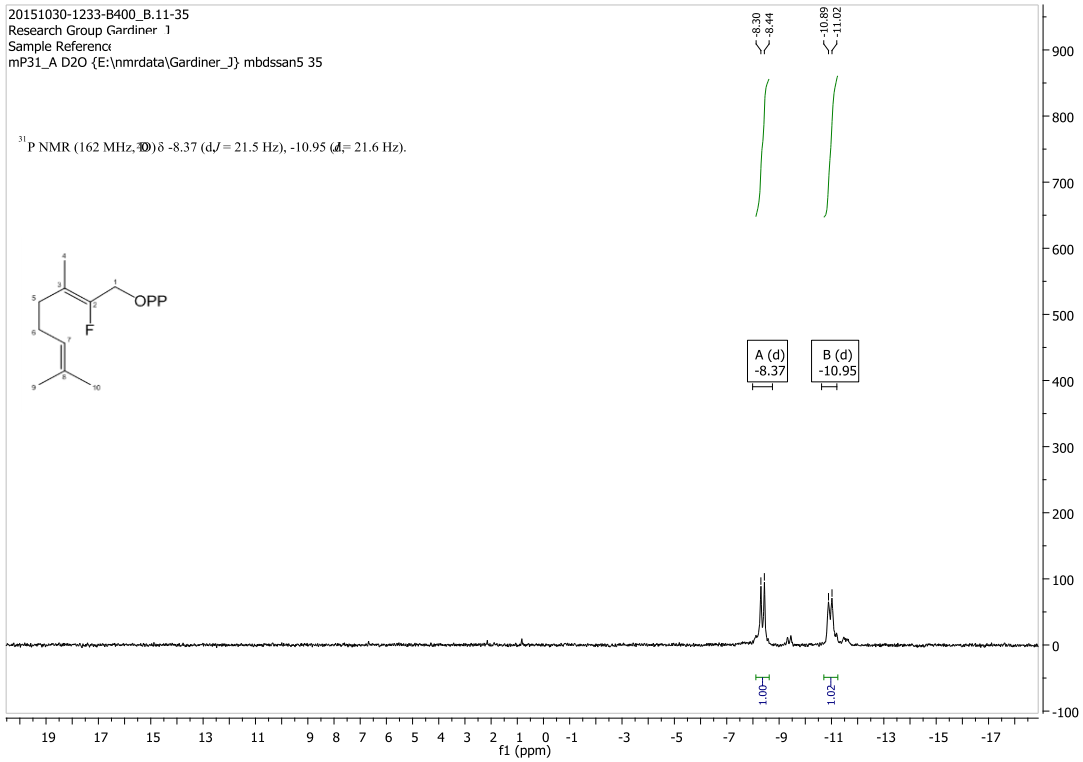
20151030-1233-B400_B.11-35
Research Group Gardiner 1
Sample Reference
mP31_A D2O {E:\nmrdata\Gardiner_J} mbdssan5 35
31P NMR (162 MHz, D2O) δ -8.37 (d, J = 21.5 Hz), -10.95 (d, J = 21.6 Hz).
-8.30
-8.44
-10.89
-11.02
OPP
F
A (d)
-8.37
B (d)
-10.95
1.00
1.02
f1 (ppm)

F

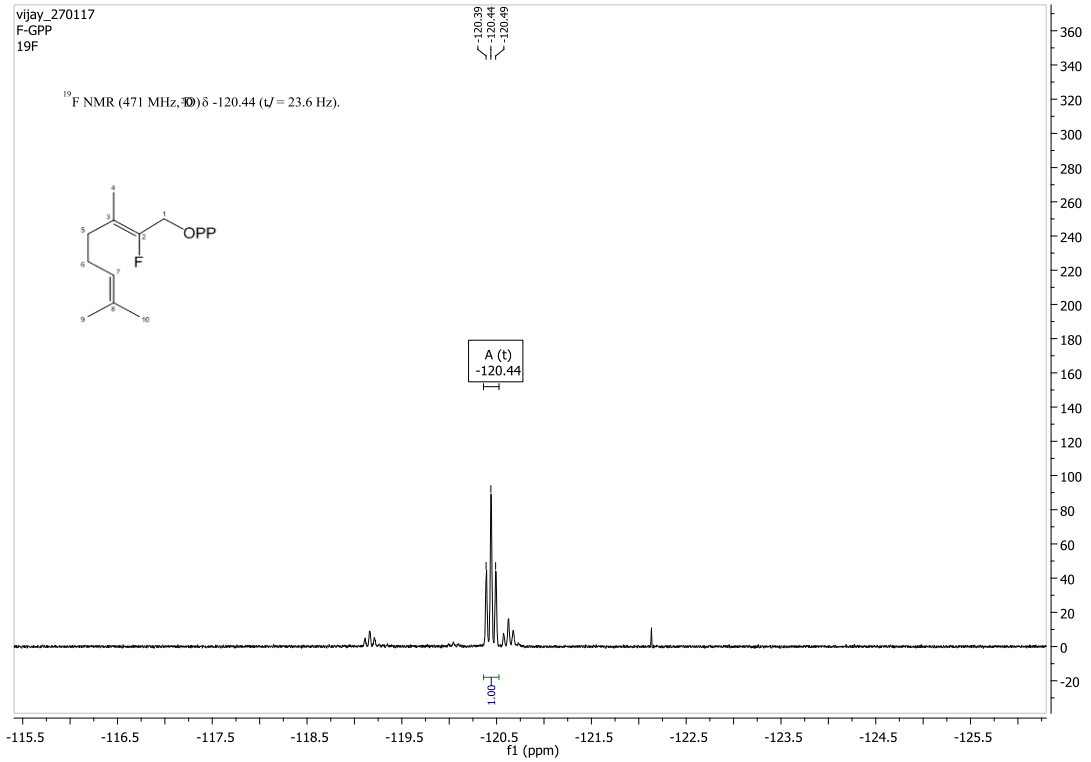
vijay_270117
F-GPP
19F
19F NMR (471 MHz, D2O) δ -120.44 (t, J = 23.6 Hz).
-120.39
-120.44
-120.49
OPP
F
A (t)
-120.44
1.00
f1 (ppm)

G

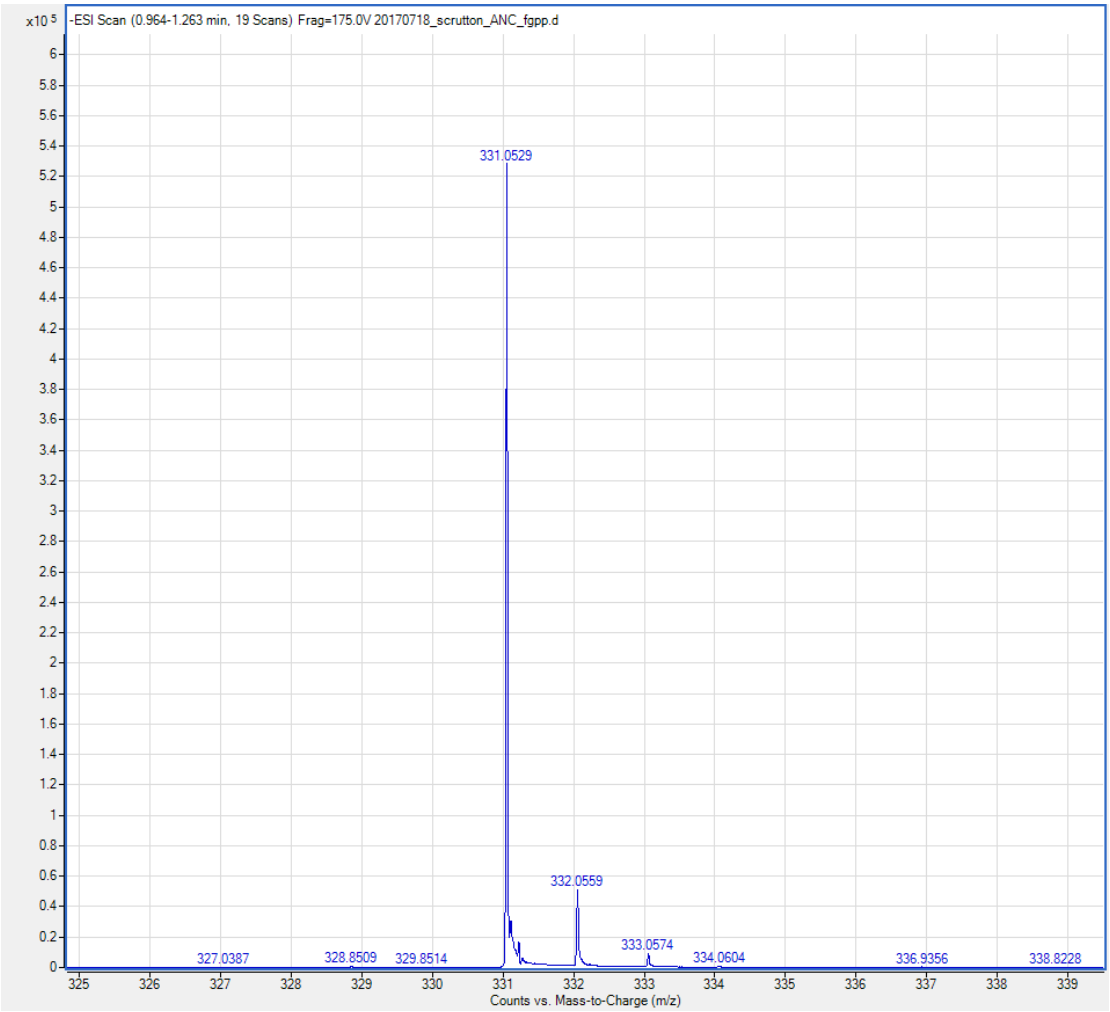

Figure S3. NMR and HRMS-ESI spectra of 2-fluorogeranyl pyrophosphate (FGPP). A) ^{1}H NMR. B) ^{13}C NMR. C) ^{1}H -^{1}H COSY. D) ^{1}H -^{13}C HSQC. E) ^{31}P NMR. F) ^{19}F NMR. G) HRMS-ESI.

A

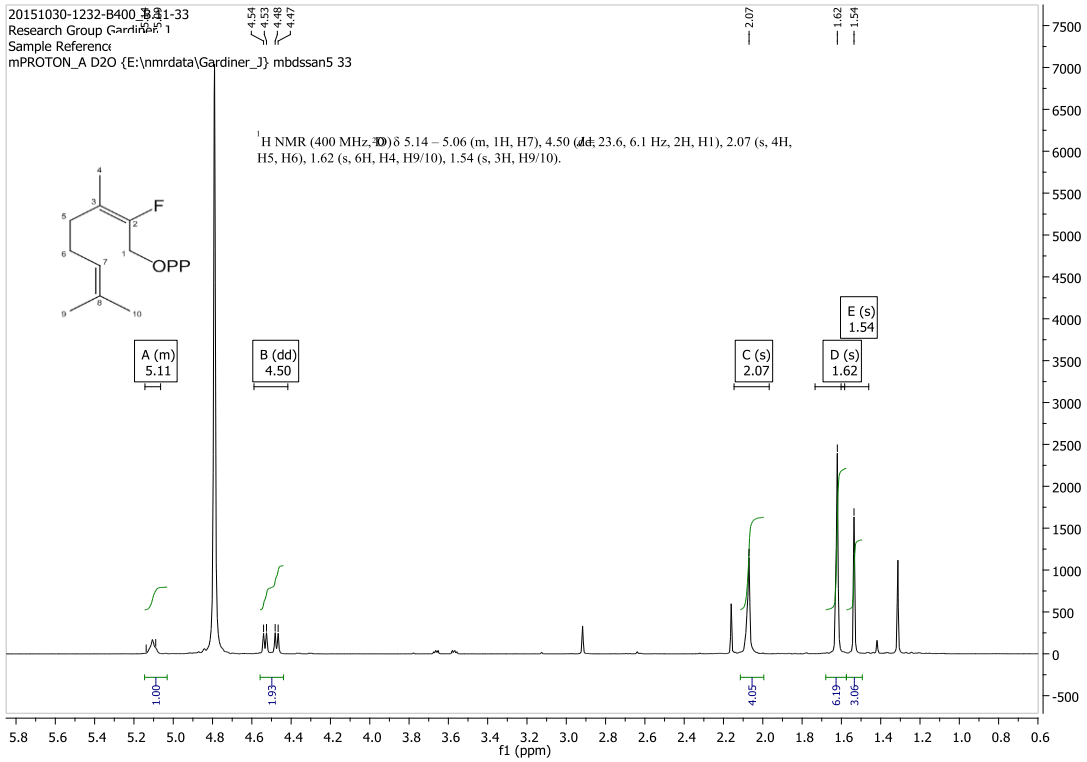
20151030-1232-B400_5_31-33
Research Group Gardiner_J
Sample Reference
mPROTON_A D2O {E:\nmrdata\Gardiner_J} mbdssan5 33
4.54
4.53
4.48
4.47
2.07
1.62
1.54
1H NMR (400 MHz, D2O) δ 5.14 – 5.06 (m, 1H, H7), 4.50 (dd, J = 23.6, 6.1 Hz, 2H, H1), 2.07 (s, 4H, H5, H6), 1.62 (s, 6H, H4, H9/10), 1.54 (s, 3H, H9/10).
F
OPP
A (m) 5.11
B (dd) 4.50
C (s) 2.07
D (s) 1.62
E (s) 1.54
1.00
1.93
4.09
6.19
3.06
f1 (ppm)

B

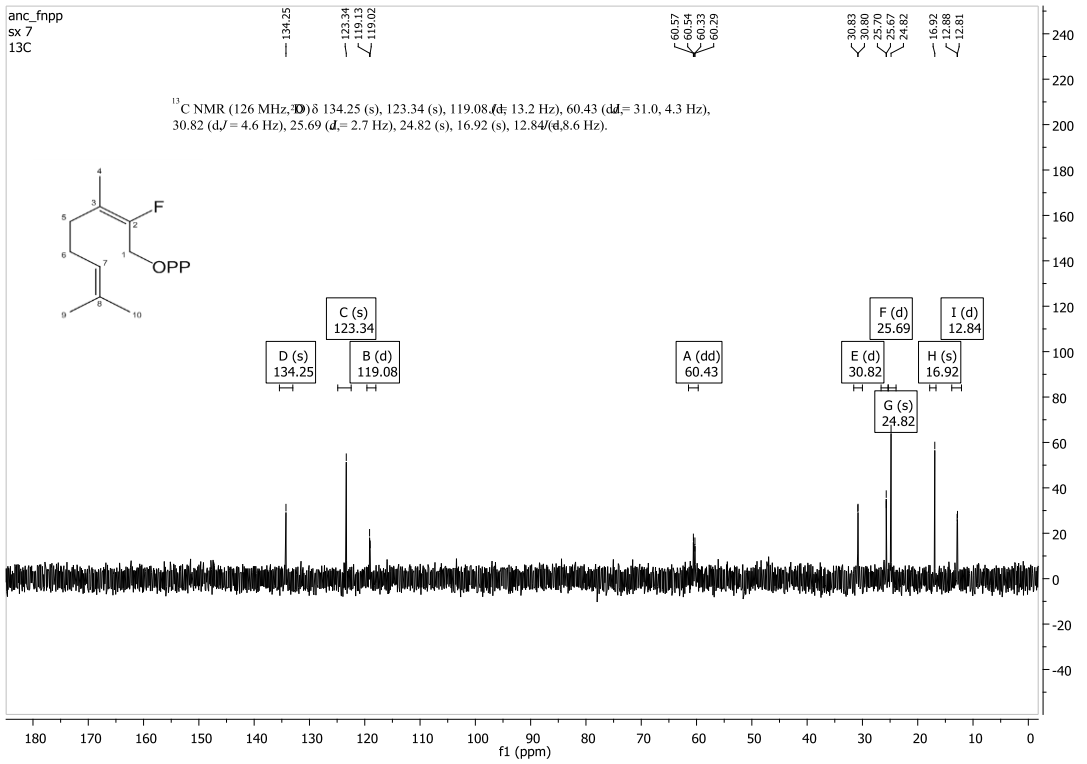
anc_fnpp
sx 7
13C
134.25
123.34
119.13
119.02
60.57
60.54
60.33
60.29
30.83
30.80
25.70
25.67
24.82
16.92
12.88
12.81
13C NMR (126 MHz, D2O) δ 134.25 (s), 123.34 (s), 119.08 (d, J = 13.2 Hz), 60.43 (dd, J = 31.0, 4.3 Hz), 30.82 (d, J = 4.6 Hz), 25.69 (d, J = 2.7 Hz), 24.82 (s), 16.92 (s), 12.84 (d, J = 8.6 Hz).
F
OPP
D (s) 134.25
C (s) 123.34
B (d) 119.08
A (dd) 60.43
E (d) 30.82
F (d) 25.69
G (s) 24.82
H (s) 16.92
I (d) 12.84
f1 (ppm)

C

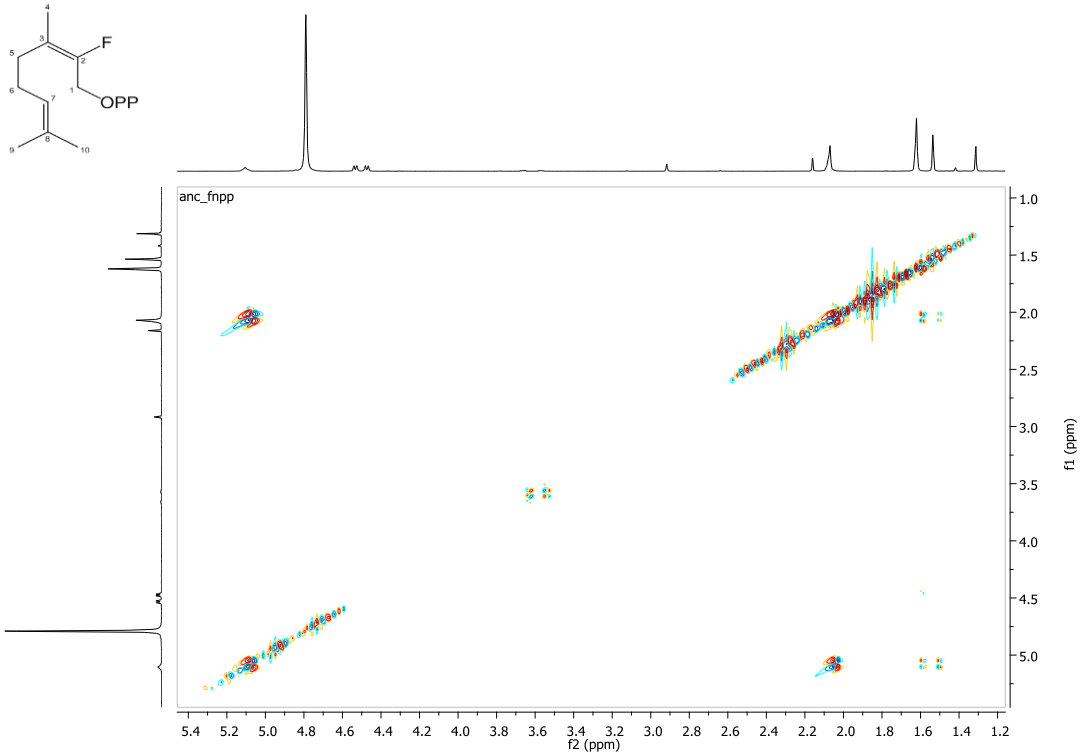

D

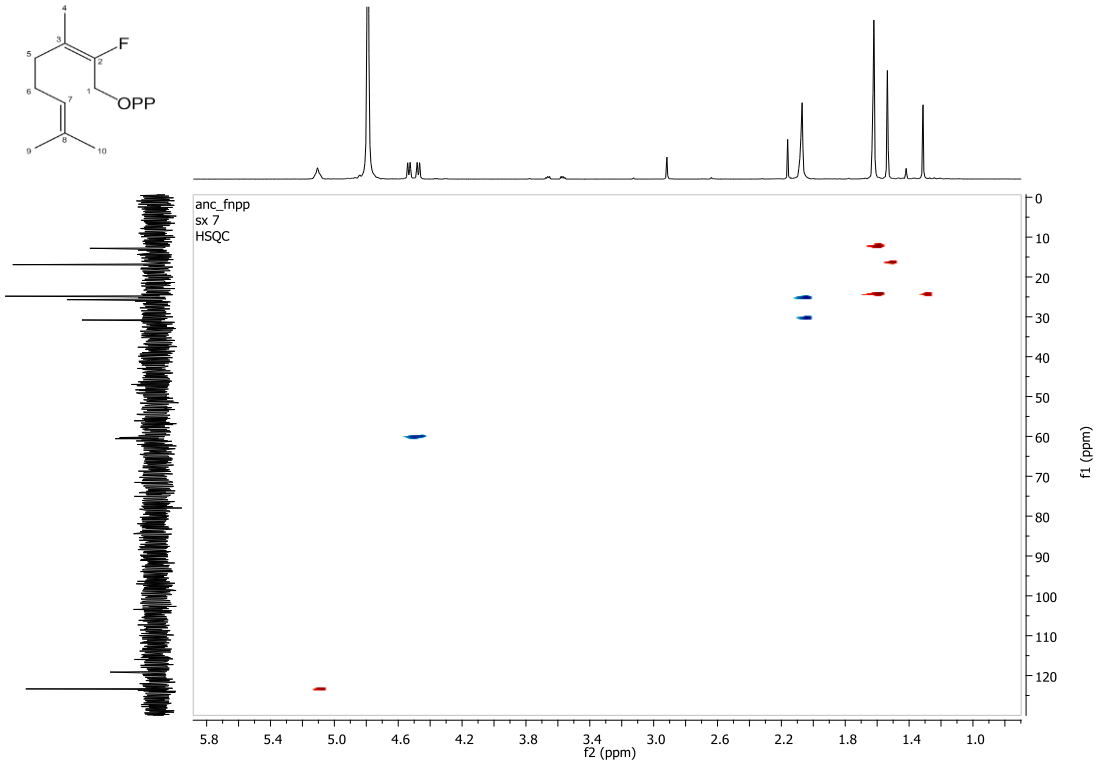

E

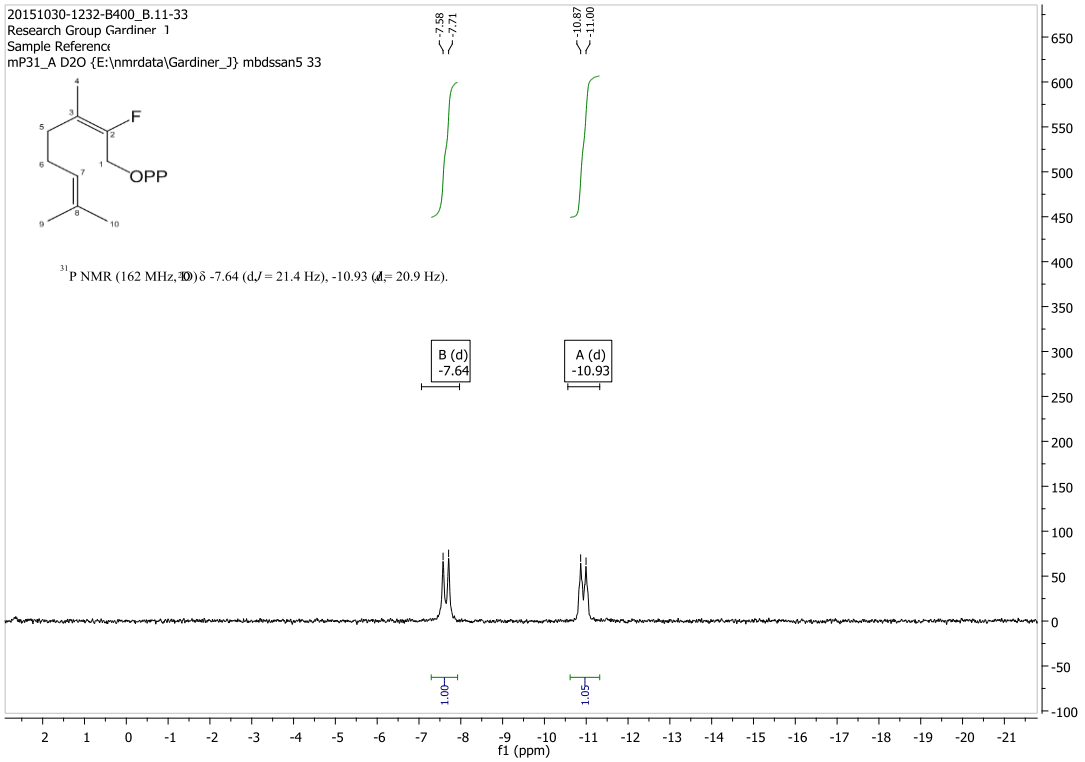

^{31}P NMR (162 MHz, D_2O) δ -7.64 (d, J = 21.4 Hz), -10.93 (d, J = 20.9 Hz).

F

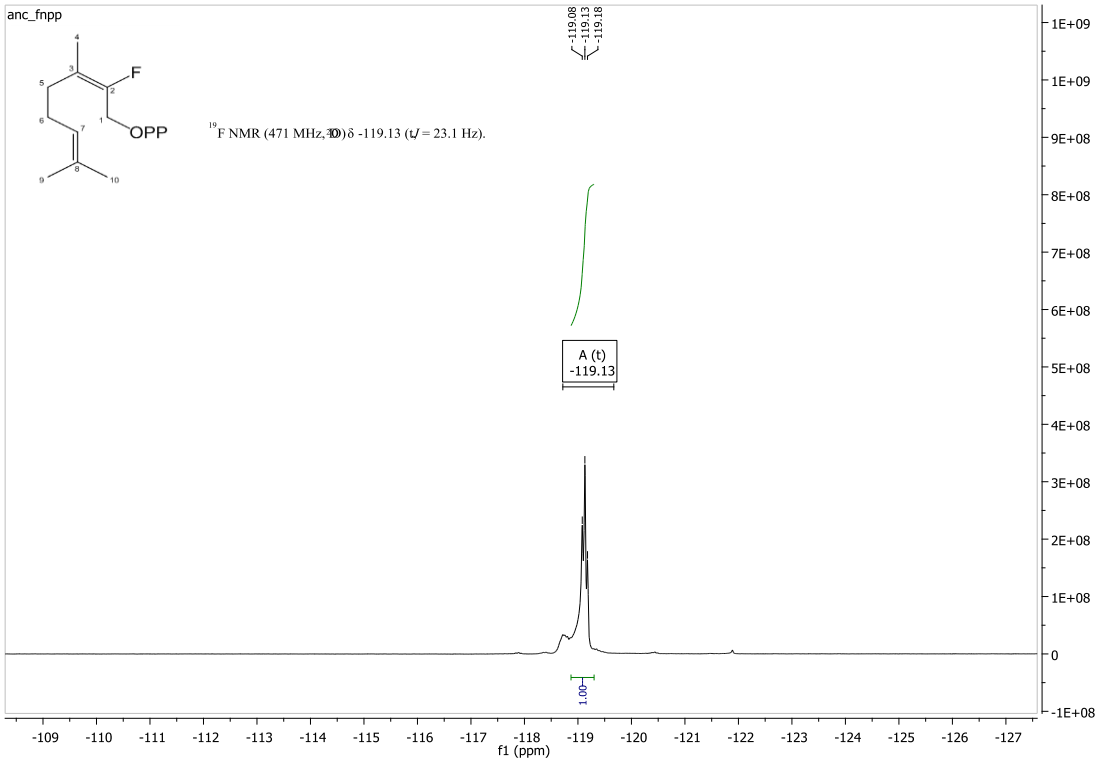

^{19}F NMR (471 MHz, D_2O) δ -119.13 (t, J = 23.1 Hz).

G

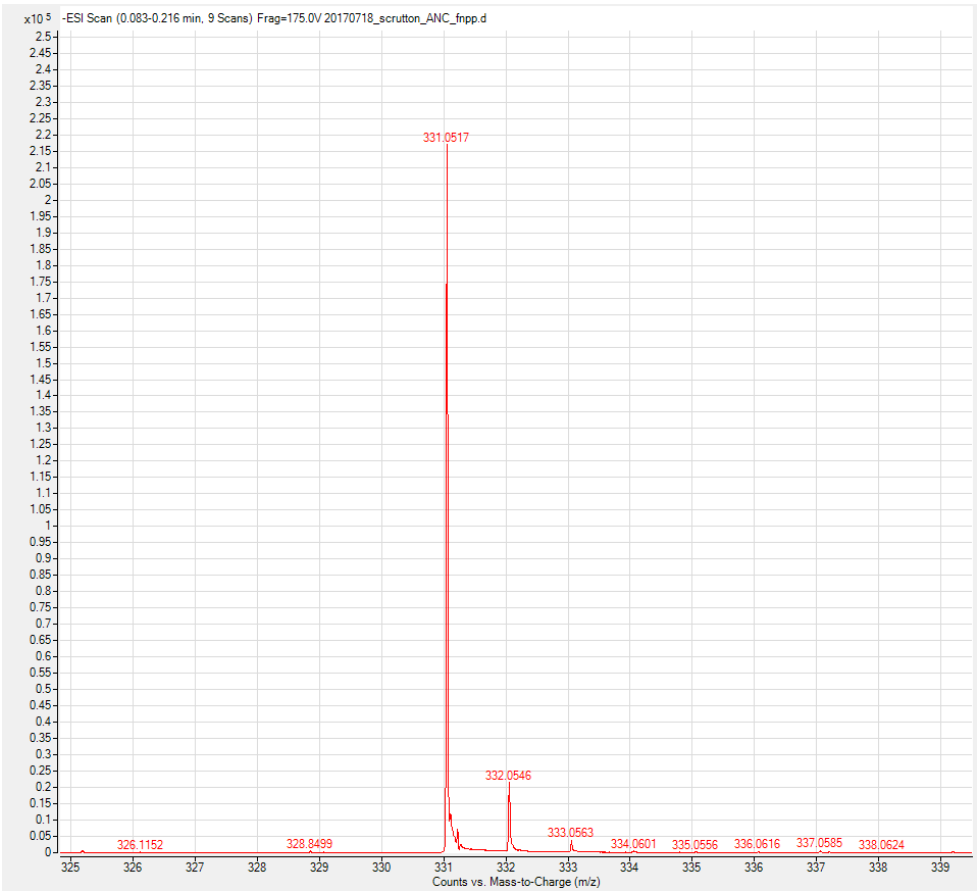
x10 5
-ESI Scan (0.083-0.216 min, 9 Scans) Frag=175.0V 20170718_scrutton_ANC_fnpp.d
331.0517
332.0546
333.0563
326.1152
328.8499
334.0601
335.0556
336.0616
337.0585
338.0624
Counts vs. Mass-to-Charge (m/z)

H

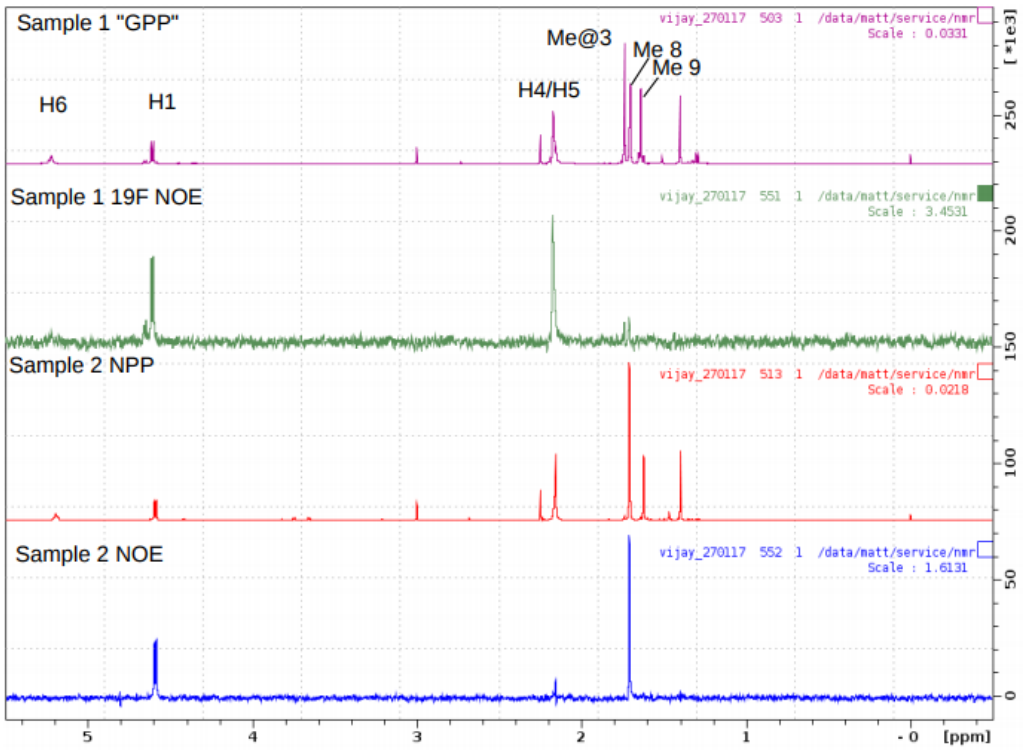

Figure S4. NMR and HRMS-ESI spectra of 2-fluoroneryl pyrophosphate (FNPP). A) ^{1}H NMR. B) ^{13}C NMR. C) ^{1}H -^{1}H COSY. D) ^{1}H -^{13}C HSQC. E) ^{31}P NMR. F) ^{19}F NMR. G) HRMS-ESI. H) Comparison of NOE data for FGPP and FNPP.

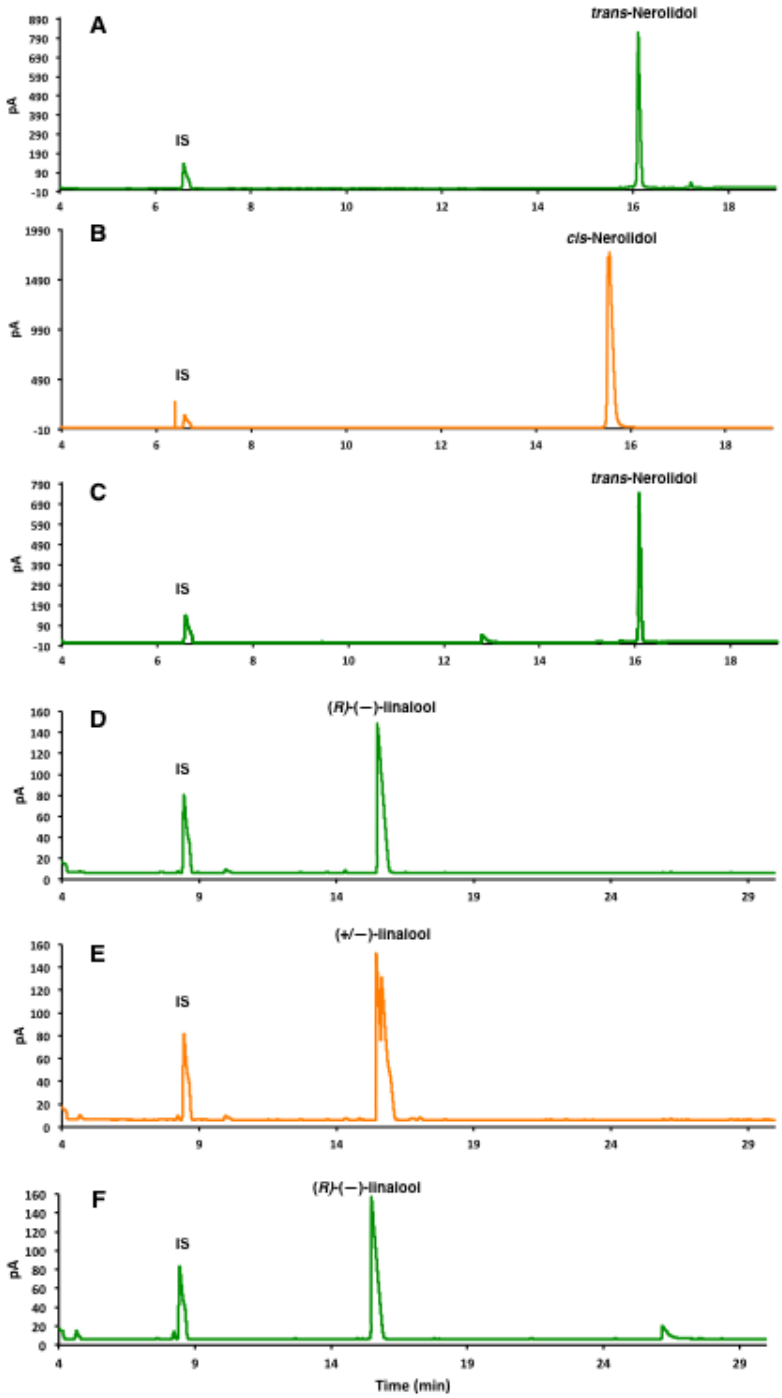

Figure S5. Gas chromatography analysis of bLinS with FPP and GPP. A) *trans*-Nerolidol standard. B) *cis*-Nerolidol standard. C) bLinS conversion of FPP (2 mM) *in vitro*. D) *R*-(–)-linalool standard. E) (+/–)-linalool standard. F) bLinS conversion of GPP (2 mM) *in vitro*. IS= internal standard (*sec*-butyl benezene)

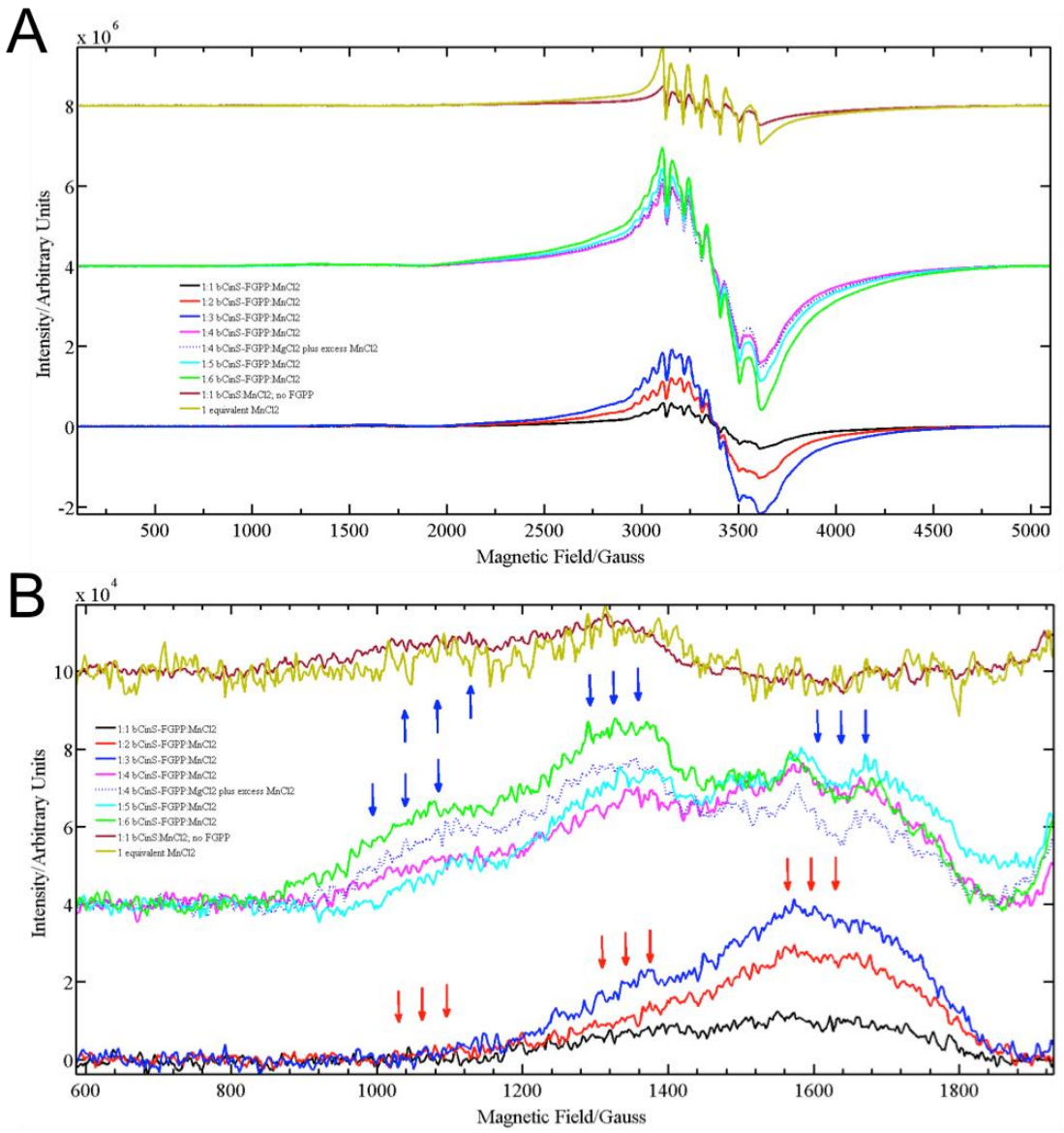

Figure S6. **cw-EPR spectra of bCinS.** Mn^{2+} substituted bCinS samples with varying equivalents of Mn^{2+} ion concentration with and without FGPP, measured as a frozen solution along with standard $MnCl_2$. A) Wide sweep from 10-510 mT. B) Expanded between 60-190 mT to show the half-field transitions of the Mn^{2+} ion under different coordination environments. The features that are highlighted with red and blue arrows are discussed in the text. Conditions: microwave power 36 dB; modulation amplitude 5 G; time constant 41 ms; conversion time 41 ms; sweep time 84 s; receiver gain 60 dB; average microwave frequency 9.384 GHz; temperature 20 K.

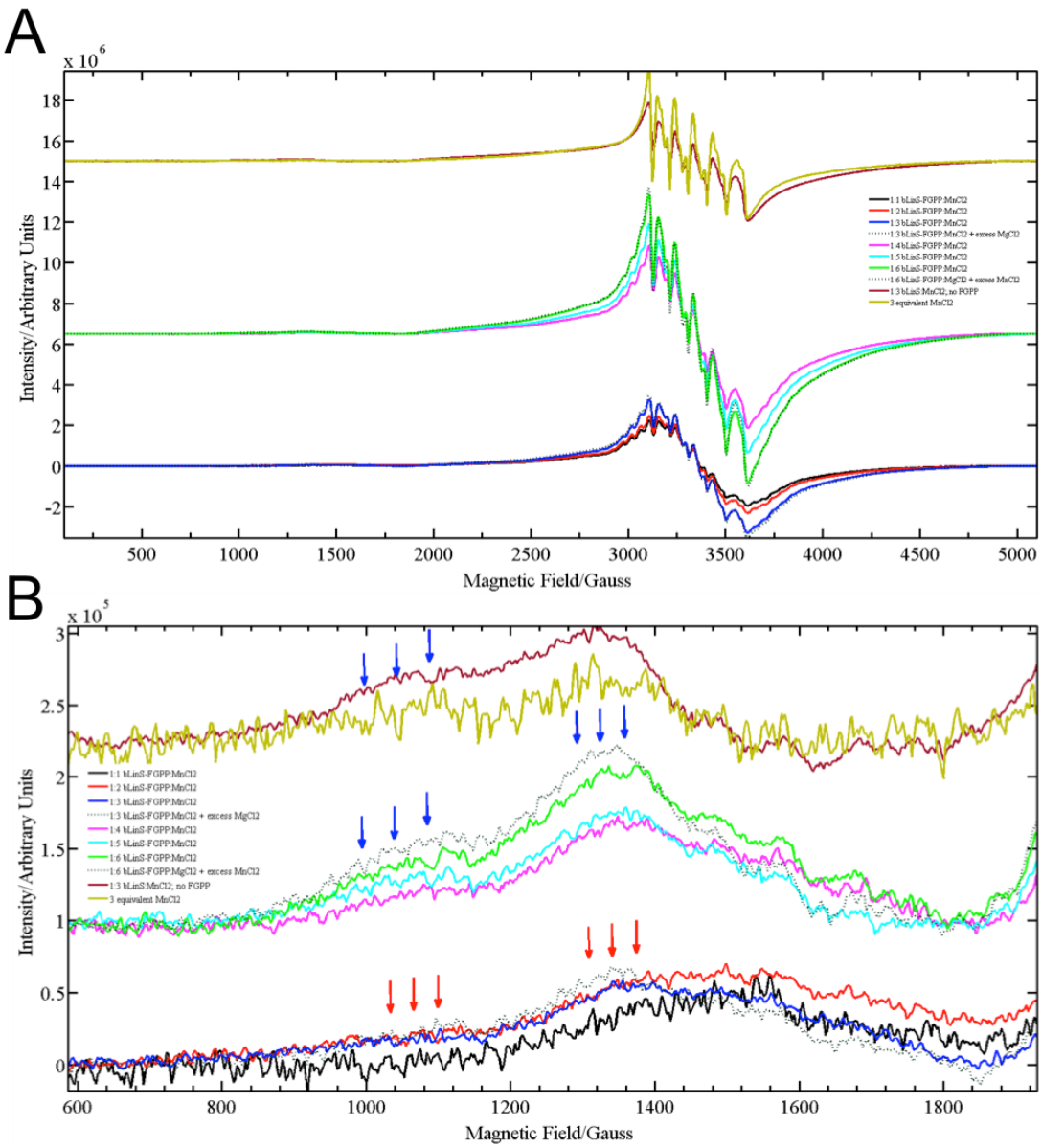

Figure S7. **cw-EPR spectra of bLinS.** Mn^{2+} substituted bLinS samples with varying equivalents of Mn^{2+} ion concentration with and without FGPP, measured as a frozen solution along with standard $MnCl_2$. A) Wide sweep from 10-510 mT. B) Expanded between 60-190 mT to show the half-field transitions of the Mn^{2+} ion under different coordination environments. The features that are highlighted with red and blue downward arrows are discussed in the text. Conditions: as in **Fig S2.**

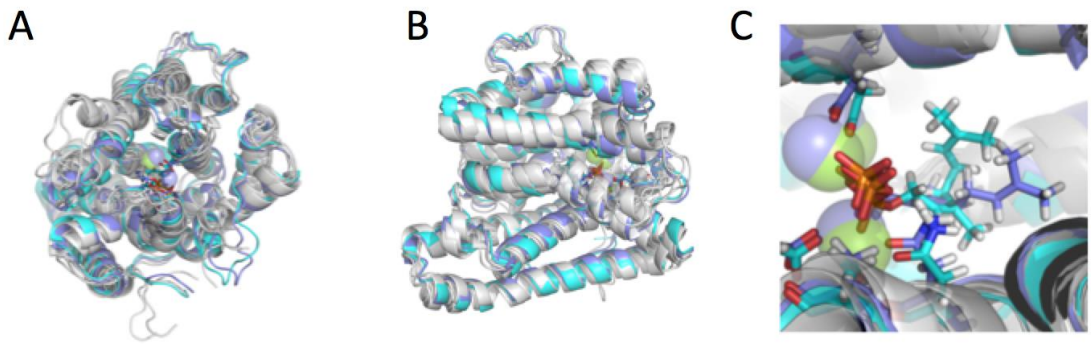

Figure S8. Comparison of structures from MD of *apo*-bCinS with MD of the ternary complex of bCinS with 3 Mg^{2+} ions and GPP or NPP. White: 4 clusters from 100 ns simulation of *apo*-bCinS, purple: the representative structure of the most populated cluster (after alignment on active site residues) from 100 ns simulations of bCinS with 3 Mg^{2+} ions and GPP, cyan the representative structure of the most populated cluster (after alignment on active site residues) from 100 ns simulations of bCinS with 3 Mg^{2+} ions and NPP. **A)** and **B)** show different views of the entire monomer, and **C)** shows the active site of bCinS. No significant structural changes are observed between the *apo* form and the ternary complex.

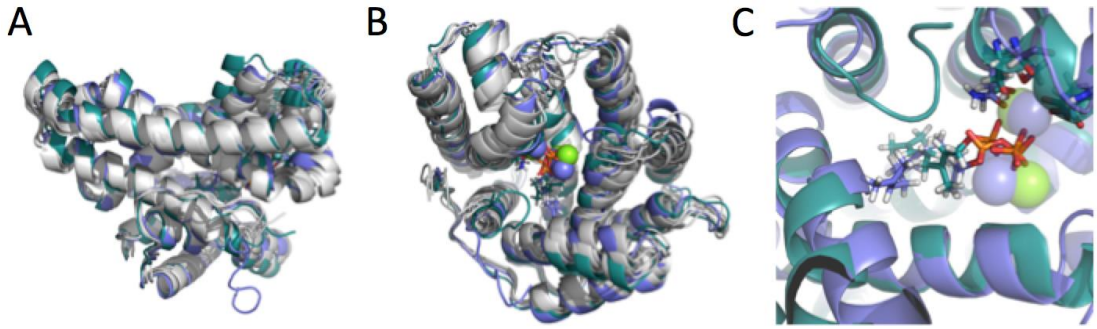

Figure S9. Comparison of structures from MD of *apo*-bLinS with MD of the ternary complex of bLinS with 3 Mg^{2+} ions and GPP or FPP. White: 4 clusters from 100 ns simulation of *apo*-LinS, teal: the representative structure of the most populated cluster (after alignment on active site residues) from 100 ns simulations of bLinS with 3 Mg^{2+} ions and GPP, purple: the representative structure of the most populated cluster (after alignment on active site residues) from 100 ns simulations of bLinS with 3 Mg^{2+} ions and FPP. **A)** and **B)** show different views of the entire monomer, and **C)** shows the active site of bLinS. No significant structural changes are observed between the *apo* form and the ternary complex. The larger FPP can easily be accommodated in the active site without any major structural rearrangements.

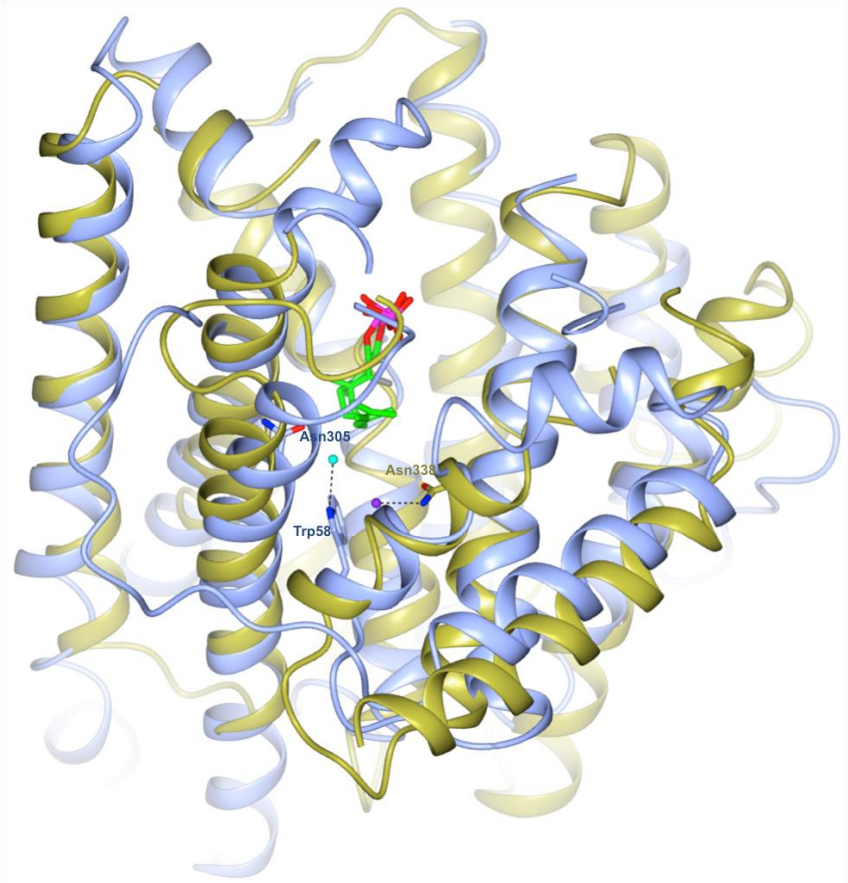

Figure S10: Structural overlay of bCinS and C-terminal domain of Sf-CinS1. In the bCinS-FNPP/FGPP structure (blue ribbon), residues Trp58 and Asn305 coordinate the water molecule (cyan sphere), which is proposed to be involved in water attack. In Sf-CinS1 (gold ribbon), Asn338 was identified to be crucial for 1,8-cineole synthesis and forms a hydrogen bond with a water molecule (purple sphere). Asn338 in Sf-CinS1 resides in a different helix and region of the active site compared to Asn305 in bCinS.

Table S1: Plasmids used in this study

Plasmid reference	**Plasmid name**	**Description (Origin of replication, Antibiotic marker, Reference(s), Promoters and Operons)**	**Reference**
pMVA	BbA5a-MTSAe-T1f-MBI(f)-T1002i	p15A, Kanr, PlacUV5, MTSA, T1, MBI-f, T1002	1
pGPPSmTC/S15	pBbB2a-trAgGPPS(co)-trSLimS_Ms	pBBR, Ampr, Ptet, trAgGPPS(co)- trSLimS_Ms	1
pGPPSmTC/S38	pBbB2a-trAgGPPS(co)-bLinS	pBBR, Ampr, Ptet, trAgGPPS(co)- bLinS	This study
pGPPSmTC/S39	pBbB2a-trAgGPPS(co)-bCinS	pBBR, Ampr, Ptet, trAgGPPS(co)- bCinS	This study

Table S2: bLinS and bCinS: homologous structures

Name	PDB	Organism	RMSD (Å) / Cα atoms
bLinS (chain A)			
Pentalenene synthase	1ps1	*Streptomyces exfoliatus*	1.52 / 283
Germacradien-4-ol synthase	5i1u	*Streptomyces citricolor*	1.59 / 276
Hedycaryol synthase	4mc3	*Actinomycete K. setae*	1.99 / 275
Geosmin synthase	5dz2	*Streptomyces coelicolor*	1.82 / 279
Epi-isozizaene synthase	4ltv	*Streptomyces coelicolor*	2.19 / 286
Selinadiene synthase	4okz	*Streptomyces pristinaespiralis*	1.83 / 265
2-Methylisoborneol synthase	4la6	*Streptomyces coelicolor*	2.09 / 268
bCinS			
Geosmin synthase	5dz2	*Streptomyces coelicolor*	1.54 / 296
Pentalenene synthase	1ps1	*Streptomyces exfoliatus*	1.80 / 292
Germacradien-4-ol synthase	5i1u	*Streptomyces citricolor*	1.80 / 283
Epi-isozizaene synthase	3kb9	*Streptomyces coelicolor*	1.94 / 304
Hedycaryol synthase	4mc3	*Actinomycete K. setae*	2.07 / 276
Aristolochene synthase	4kwd	*Aspergillus terreus*	2.28 / 280

REFERENCES

1. Leferink, N. G. H.; Jervis, A. J.; Zebec, Z.; Toogood, H. S.; Hay, S.; Takano, E.; Scrutton, N. S. *ChemistrySelect* **2016,** 1, 1893-1896.